

**Contract No.:**

This manuscript has been authored by Savannah River Nuclear Solutions (SRNS), LLC under Contract No. DE-AC09-08SR22470 with the U.S. Department of Energy (DOE) Office of Environmental Management (EM).

**Disclaimer:**

The United States Government retains and the publisher, by accepting this article for publication, acknowledges that the United States Government retains a non-exclusive, paid-up, irrevocable, worldwide license to publish or reproduce the published form of this work, or allow others to do so, for United States Government purposes.

## Accepted Manuscript

Growth of CdMnTe free of large Te inclusions using the vertical Bridgman technique

U.N. Roy, G.S. Camarda, Y. Cui, R. Gul, A. Hossain, G. Yang, O.K. Okobiah, S.U. Egarevwe, R.B. James

PII: S0022-0248(18)30638-9

DOI: <https://doi.org/10.1016/j.jcrysgro.2018.12.026>

Reference: CRYG 24900

To appear in: *Journal of Crystal Growth*

Received Date: 5 December 2018

Accepted Date: 23 December 2018

Please cite this article as: U.N. Roy, G.S. Camarda, Y. Cui, R. Gul, A. Hossain, G. Yang, O.K. Okobiah, S.U. Egarevwe, R.B. James, Growth of CdMnTe free of large Te inclusions using the vertical Bridgman technique, *Journal of Crystal Growth* (2018), doi: <https://doi.org/10.1016/j.jcrysgro.2018.12.026>



This is a PDF file of an unedited manuscript that has been accepted for publication. As a service to our customers we are providing this early version of the manuscript. The manuscript will undergo copyediting, typesetting, and review of the resulting proof before it is published in its final form. Please note that during the production process errors may be discovered which could affect the content, and all legal disclaimers that apply to the journal pertain.

**Growth of CdMnTe free of large Te inclusions using the vertical Bridgman technique**

U. N. Roy<sup>1\*</sup>, G. S. Camarda<sup>1</sup>, Y. Cui<sup>1</sup>, R. Gul<sup>1,2</sup>, A. Hossain<sup>1</sup>, G. Yang<sup>1\*\*</sup>, O. K. Okobiah<sup>1,2</sup>, S.

U. Egarevwe<sup>1,2</sup>, and R. B. James<sup>1†</sup>

<sup>1</sup>Brookhaven National Laboratory, Upton, NY 11973, USA

<sup>2</sup>Alabama A&M University, Normal, AL 35762, USA

<sup>†</sup>Present address: Savannah River National Laboratory, Aiken, SC 29808, USA

<sup>\*\*</sup>Present address: North Carolina State University, Raleigh, NC 27695-7909, USA

**Abstract**

We grew Cd<sub>1-x</sub>Mn<sub>x</sub>Te crystals with a nominal composition of 5% Mn and 95% Cd using the vertical Bridgman technique. We were able to grow crystals from as-received starting material that were free of secondary phases, such as Te inclusions with a size > 1-μm diameter, without adding compensating Cd to the initial charge. The Te precipitations (size < 1-μm diameter) were found to segregate towards the last-to-freeze section of the ingot. Te inclusions with a size 5-7 μm were observed at the grain boundary located near the last-to-freeze section, while the bottom and middle parts of the ingot showed no Te inclusions, even at the grain boundaries. X-ray topographic analysis was used to characterize the distribution of thermal stress in the ingot.

\*E-mail address: [uroy@bnl.gov](mailto:uroy@bnl.gov)

## 1. Introduction

$\text{Cd}_{1-x}\text{Mn}_x\text{Te}$  (CMT) is perhaps the most widely used material in the family of ternary II-V compounds due to its wide range of applications. The material has long been known as a diluted magnetic semiconductor [1,2] for the range of Mn concentration ranging from  $x = 0.0$ - $0.77$ . Because of the magnetic and magneto-optic properties, CMT offers several applications such as Faraday rotator viz. optical isolator and magnetic field sensors [3-7]. Due to the wide tunability of the lattice constant with varying Mn concentration, CMT has also been used as a lattice-matched substrate material for  $\text{Hg}_{1-x}\text{Cd}_x\text{Te}$  for infrared (IR) detector applications [8-10]. CMT has also been reported to be a promising material for X- and gamma-ray detectors operable at room temperature [11-14]. From the material properties standpoint, CMT has some potential advantages over commonly used  $\text{CdZnTe}$  for X- and gamma-ray detection. For  $\text{Cd}_{1-x}\text{Mn}_x\text{Te}$ , the band-gap increases about 13 meV per atomic percent of Mn, while for  $\text{Cd}_{1-x}\text{Zn}_x\text{Te}$ , the corresponding value is 6.7 meV, so less Mn is required to achieve a desired band-gap [12]. Another main advantage is the near-unity segregation coefficient of Mn in CdTe matrix [8, 9], as compared to the segregation coefficient of Zn in CdTe matrix, which is about 1.35 [15]. Thus, CMT crystals can be grown with higher axial compositional homogeneity than CZT, resulting in a potential lower cost of production for large-volume detectors.

Regarding defects in CZT and CMT crystals, the presence of Te inclusions/precipitations, commonly known as Te-rich secondary phases, has continued to be a major drawback for fabricating high-performance devices for all the applications mentioned above. For optical devices, Te inclusions in the CZT/CMT matrix cause severe scattering centers. For IR substrate applications, Te inclusions exposed on the surface of the substrate have an adverse effect on the quality of the  $\text{Hg}_{1-x}\text{Cd}_x\text{Te}$  epitaxial layer due to the different lattice constant of Te and  $\text{Hg}_{1-x}\text{Cd}_x\text{Te}$ . The Te inclusions are also known to severely hinder the charge-transport characteristics

[16] of radiation detectors, causing deterioration of device performance due to pulse-height distortion.

Secondary phases are divided into two categories depending upon their origin of formation. The Te inclusions are known to originate due to a morphological instability of the growth interface. The sizes of Te inclusions are  $> 1 \mu\text{m}$ , while the Te precipitates occur due to the retrograde solubility of Te [17]. The size of the precipitations are much less than  $1 \mu\text{m}$ . The Te precipitates are best observed by transmission electron microscopy and are generally not visible via IR transmission microscopy. Although the Te inclusions can be removed by post-growth annealing in a Cd atmosphere [18], the annealing process produces large star-like defects, typically with a size of 50-100 times larger in diameter than those of the Te inclusions prior to annealing. [19]. These large star-like defects also severely hinder the charge-transport characteristics [19]. In the recent past, Swain et al. [20] demonstrated the feasibility of growing CdTe crystals by the vertical Bridgman technique that were free from Te inclusions with a size  $> 1 \mu\text{m}$ . In this paper we report the growth of CMT crystals that are free from Te inclusions with a size  $> 1 \mu\text{m}$  using the vertical Bridgman technique.

## 2. Experimental

CMT crystals with a nominal composition of 5 atomic % of Mn were grown by the vertical Bridgman configuration using a three-zone tubular furnace. The  $\text{Cd}_{0.95}\text{Mn}_{0.05}\text{Te}$  compound was synthesized from stoichiometric amounts of 6N purity CdTe procured from 5N Plus, 99.9998% pure Mn, and 6N purity Te procured from Alfa Aesar. It is worth mentioning that the CdTe raw material did contain Te inclusions as observed by IR transmission microscopy, and no additional elemental Cd was used to compensate for Cd evaporation during our growth experiments. The synthesis and growth were carried out in the same ampoule to avoid any additional unwanted

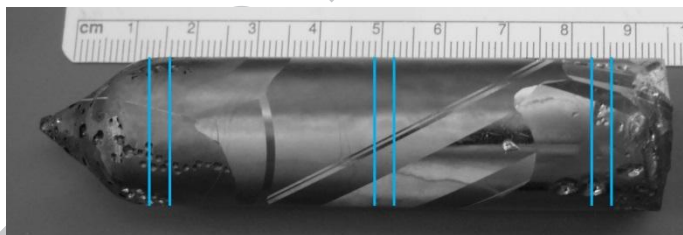
impurities. The crystals were grown in a conically tipped ampoule with the cone angle of about 70°. The inner diameter of the ampoule was 22 mm with a wall thickness of 1.9 mm. Prior to loading, the inner wall of the ampoule was coated with a graphite film by cracking spectroscopic acetone at about 900 °C, followed by vacuum annealing of the ampoule at about 1100 °C for an hour. The loaded ampoule was then sealed under a dynamic vacuum of  $\sim 2 \times 10^{-6}$  torr. The ampoule was then placed inside the three-zone vertical furnace, and the temperature of the furnace was raised to 900 °C over 24 hours. Next, the temperature was further raised to  $\sim 1110$  °C near the tip of the ampoule at a rate to  $\sim 4$  °C/hr. The loaded ampoule was kept at 1100 °C for the next 48 hours for complete synthesis, followed by lowering the ampoule at a speed of  $\sim 4$  cm/day through a temperature gradient of 7-10 °C/cm near the melt/solid interface. After completion of the crystallization, the ampoule was cooled to room temperature at a rate of  $\sim 300$  °C/day.

Upon cooling to room temperature, the ampoule was taken out from the furnace, and the ingot was removed without any problem associated with sticking to the ampoule wall. Wafers were cut perpendicular to the ingot axis at different positions from the bottom, middle and near the top of the as-grown ingot using a diamond-impregnated wire saw. The cut wafers were then lapped with SiC paper with successive different grit sizes, and then polished successively with 3  $\mu\text{m}$ , 1  $\mu\text{m}$ , 0.5  $\mu\text{m}$  grit and finally polished with a 0.05- $\mu\text{m}$  alumina suspension on a felt pad to obtain a mirror-like surface finish. High magnification infrared (IR) transmission microscopy was performed to investigate the presence of secondary phase, such as Te inclusions, in the grown ingot. White Beam X-ray Diffraction Topography (WBXDT) analyses were carried out at LBNL's Advanced Light Source (ALS) Beamline 3.3.2 with a beam energy ranging from 4 to 25 keV. For topographic measurements, the polished samples were etched in a freshly prepared 2%

bromine-methanol solution for two minutes to remove any undesired damaged layer at the surface that was introduced during the polishing process. The grain boundaries and twins were revealed by etching in a Saucedo solution [21].

### 3. Results and discussion

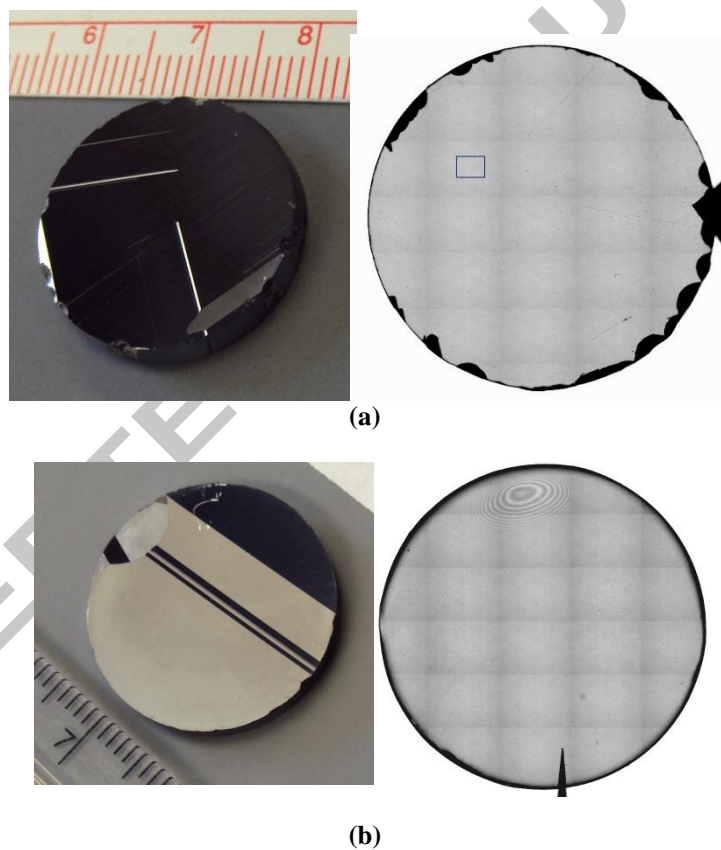
The optical photograph of the  $\text{Cd}_{0.95}\text{Mn}_{0.05}\text{Te}$  ingot grown by the vertical Bridgman technique is shown in Figure 1. The whole ingot was etched in a Saucedo solution to reveal the grain boundaries and twins. The weight of the ingot is about 178 gm, and the diameter and length is about 2.2 cm and 10 cm, respectively. Few grain boundaries and twins are visible as shown in Fig. 1. Wafers were cut perpendicular to the ingot axis from different portions of the ingot as indicated by the blue marks in Fig. 1. We investigated three wafers from top, middle and bottom portions of the ingot to analyze the secondary phase distribution. Figures 2a, 2b and 2c show the wafers with diameter of 22 mm and their corresponding IR transmission images, taken from the



**Figure 1. Optical photograph of the CMT ingot grown by the vertical Bridgman technique. The ingot was etched in a Saucedo solution. The wafers taken from the different positions are marked by blue vertical lines (not shown to scale).**

bottom, middle and top parts of the as-grown ingot. The left side image show the optical photograph of the wafers etched with a Saucedo solution, revealing the twins and the grain boundaries. More than 90% of the wafers from bottom and middle parts of the wafers are single crystalline, while a few grains were found to appear towards the top part of the ingot, as shown in Fig. 2c. The polycrystalline nature near the top part of the ingot is also revealed after etching in the Saucedo solution, as shown Fig. 1. The occurrence of smaller grains near the top part of

the ingot might be caused by an instability at the growth interface as the growth rate was relatively high ( $\sim 4$  cm/day). As mentioned, the right-side photographs of Fig. 2 are the IR transmission images of the polished wafers. The IR transmission image of the full wafer was acquired by scanning the whole wafer in transmission mode. Each square with the shaded boundary, as shown in the IR transmission image, is the field of view at a particular point. The scanned images were stitched to obtain the full image of the wafer. It is evident from the IR transmission images for all the wafers along the length of the ingot that the material is free from Te inclusions with a size  $> 1\ \mu\text{m}$ . The inclusions/precipitations with a size less than  $1\ \mu\text{m}$  are not





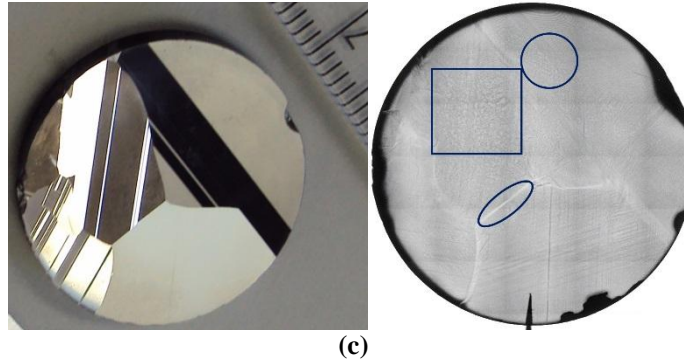


**Figure 2.** Photograph of the wafers etched with a Saucedo solution, cut perpendicular to the ingot axis (left) and the corresponding IR transmission image of the full wafer with a diameter of 22 mm cut from a) bottom, b) middle and c) top of the ingot, as indicated by the vertical blue lines in Fig. 1.

visible in the IR transmission mode due to the wavelength limitations. The wafers were also investigated under high magnification IR transmission microscopy to confirm the presence of the secondary phases. Figure 3 shows the enlarged version of the randomly chosen small rectangle indicated on Fig. 2a. Fig. 3 confirms that the material is apparently free from Te inclusions with a size of  $> 1 \mu\text{m}$ . No trace of Te inclusions was found even at very high magnification, as shown

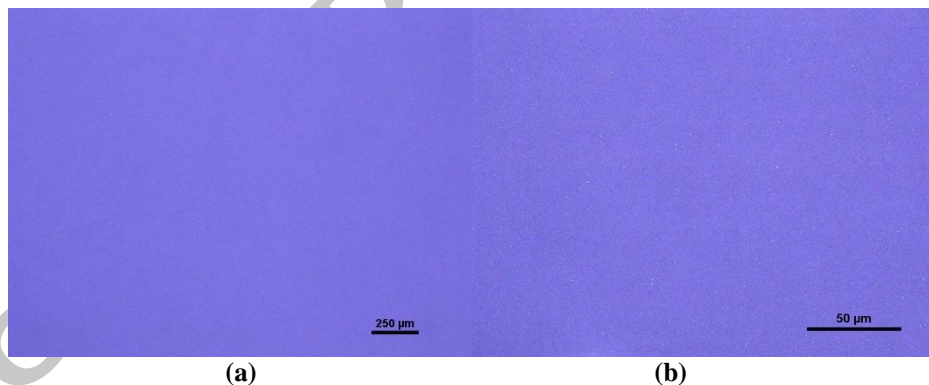


**Figure 3.** High magnification IR transmission microscopic image of  $\text{Cd}_{0.95}\text{Mn}_{0.05}\text{Te}$  sample, a) at magnification 5X and b) 50X. The bar on the right bottom of each image indicates the scale.

in Fig. 3b. To ensure the statistics, we randomly chose a smaller sample from another part of the ingot to investigate the distribution of Te inclusions. Figure 4 shows the scanning microscopic image of the sample with dimensions of  $7.9 \times 5.6 \times 3.2 \text{ mm}$  in a) reflection mode and in b) IR transmission mode. The IR transmission image evidently confirms the absence of any Te

inclusions with sizes  $> 1 \mu\text{m}$ . Figure 5 (a, b, c and d) shows a series of high magnification IR transmission microscopic images focused at different depths of the sample at an arbitrary



**Figure 4.** Microscopic scanning image of the  $\text{Cd}_{0.95}\text{Mn}_{0.05}\text{Te}$  sample, a) in reflection mode and b) in IR transmission mode. Sample dimensions:  $7.9 \times 5.6 \times 3.2 \text{ mm}^3$ .

position in Fig. 4b. Fig. 5a shows the IR transmission microscopic image near the surface of the sample. The polishing scratches are visible, while Figs. 5(b-c) are the same images at different depths of the sample. No trace of Te inclusions with a size  $> 1 \mu\text{m}$  were detected as is also evident from Fig. 5. Recently Swain et al. [20] demonstrated production of inclusion-free CdTe ingots grown by the vertical Bridgman growth technique by employing a fast growth rate. Our present result for CMT growth also agrees very well with the observation by Swain et al. [20]. It is to be noted that in our study, unlike Swain et al., no excess cadmium was added to the initial charge. Thus, as opposed to the observation by Swain et al., we did not observe the presence of any star-like defects in our ingot. These star-like defects are in general visible for either samples annealed in a Cd atmosphere at temperatures exceeding the melt temperature of Te [22] or Bridgman grown ingots grown under Cd partial pressure [23].

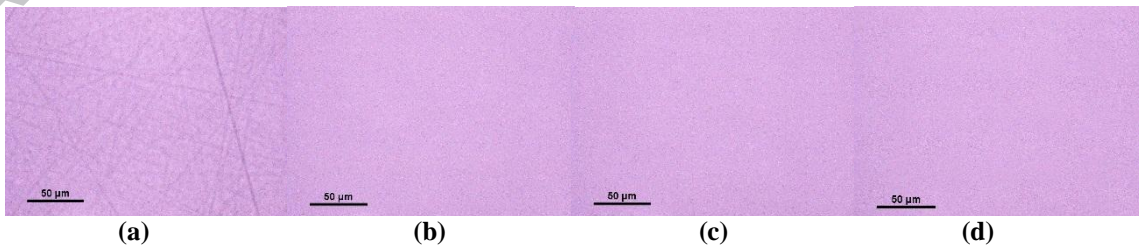


**Figure 5.** High magnification IR transmission microscopic images of the  $\text{Cd}_{0.95}\text{Mn}_{0.05}\text{Te}$  sample focused at different depths. The same magnification was used for all the images.

It is to be noted that the IR transmission image of the wafer taken from the top of the ingot, which is the last-to-freeze section (Fig. 2c), shows the presence of cloudy patches in almost the entire area of the wafer. Some of them are highlighted in the square and the circular regions indicated in Fig 2c. The enlarged version of the rectangle indicated in Fig 2c is shown in Figure 6. The appearance of the cloudy patches are possibly the coagulation of heavily segregated Te precipitations, which are  $< 1 \mu\text{m}$  in size. The Te precipitates with sizes  $< 1 \mu\text{m}$  are reported to segregate heavily towards the last-to-freeze section of the ingot [24].



**Figure 6. Enlarged version of the square indicated in Fig. 2c.**

Te inclusions, however, were observed to be present at the grain boundaries, only at the last to freeze section. Figure 7a shows the IR transmission image of a typical grain boundary at the surface of the sample. Te inclusions are visible at the grain boundary. Figure 7b shows the same grain boundary at a depth below the surface, while Fig. 7c shows the same area at higher magnification showing the size of the Te inclusions. Very few Te inclusions were found to be present at the grain boundary; they were observed to be slightly elongated with a size varying between  $5\text{--}7 \mu\text{m}$ . In the ingots grown with conventional growth sequence, the grain boundaries were observed to be heavily decorated with Te inclusions [25].

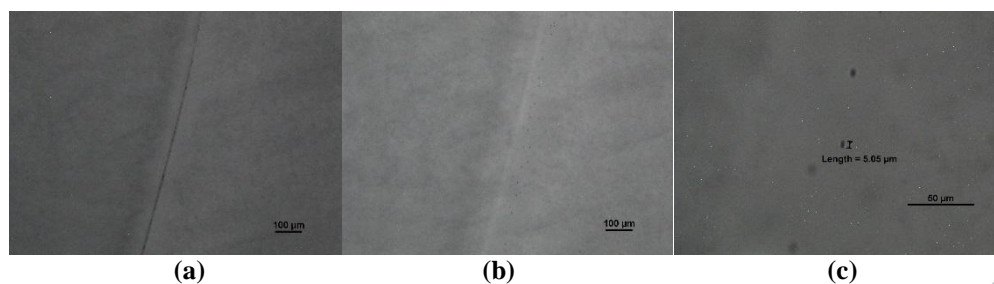


**Figure 7.** High magnification IR transmission microscopic image of the grain boundary, a) focused on the surface, b) focused at a depth along the grain boundary, and c) higher magnification image focused below the surface along the grain boundary, indicating the size of the Te inclusions.

The structural quality of the ingot was evaluated by Synchrotron White Beam X-ray Diffraction Topography (WBXDT) in the reflection mode. Figure 8 shows an X-ray topographic image of the whole wafer taken from the middle of the ingot (wafer shown in Fig. 2b). As evident from Fig. 8, the periphery of the topographic image is deformed from the circular periphery of the wafer. This in general indicates the presence of thermal stress in the wafer. The wafer was found to be highly decorated with sub-grain boundaries and their network, possibly caused by thermal stress introduced during the fast growth and fast cooling processes. Very less thermal stress and sub-grain boundaries however was observed for the conventionally grown CMT ingot [25].

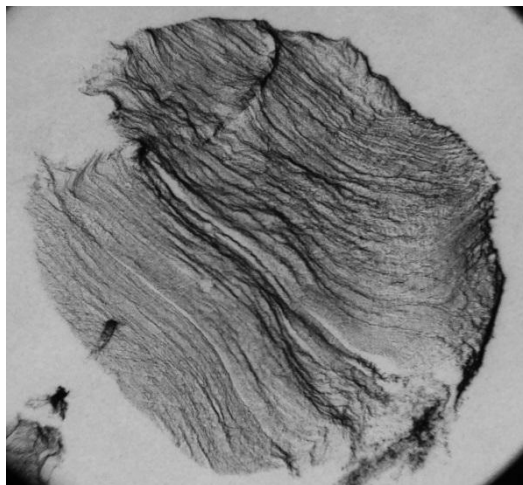


**Figure 8.** X-ray topographic image of the whole wafer shown in Fig. 2b.

#### 4. Summary

We grew  $\text{Cd}_{1-x}\text{Mn}_x\text{Te}$  crystals with a nominal composition of 5% Mn and 95% Cd by the vertical Bridgman technique. Our results show that the crystals are free from Te inclusions with a size  $> 1 \mu\text{m}$ . The crystals were grown from as-received material without adding any compensating excess Cd. We have successfully demonstrated that the fast growth and fast cooled ingots result in achieving ingots free from secondary phases that could be detected by IR transmission. Even with our fast growth process, the grain size of the ingot is very large except for the last-to-freeze section of the ingot, which is very encouraging for producing large-grain CMT ingots free from secondary phases at a cheaper cost of production compared to CZT. The crystals however did reveal the presence of some thermal stress as was observed by X-ray topographic analysis.

#### Acknowledgments

This work has been supported by the U.S. Department of Homeland Security, Domestic Nuclear Detection Office, under competitively awarded contract/IAA award number 2012-DN-077-ARI065-03. Alabama A&M University researchers were also supported by the U.S. Nuclear Regulatory Commission through award number NRC-27-10- 514. BNL scientists received support from the U.S. Department of Energy's Office of Defense Nuclear Nonproliferation Research and Development, NA-22. This support does not constitute an expressed or implied endorsement by the U.S. Government. The manuscript has been authored by Brookhaven Science Associates, LLC under Contract No. DE-AC02-98CH1-886 with the U.S.

**References:**

1. L. A. Kolodziejski, T. C. Bonsett, R. L. Gunshor, S. Datta, R. B. Bylsma, W. M. Becker, and N. Otsuka, *Appl. Phys. Lett.* 45 (1994) 440.
2. J. K. Furdyna, *J. Appl. Phys.* 64 (1988) R29.
3. A. E. Turner, R. L. Gunshor, and S. Datta, *Appl. Opt.* 22 (1983) 3152.
4. D. U. Bartholomew, J. K. Furdyna, A. K. Ramdas, *Phys. Rev. B* 34 (1986) 6943.
5. D. L. Peterson, A. Petrou, M. Datta, A. K. Ramdas, S. Rodriguez, *Solid State Commun.* 43 (1982) 667.
6. R. R. Galazka, S. Nagata, P. H. Keesom, *Phys. Rev. B* 22 (1980) 3344.
7. H. Guerrero, J. L. Escudero and E. Bernabeu, *Sensors and Actuators A: Physical* 39 (1993) 25.
8. R. Triboulet, A. Heurtel and J. Rioux, *J. Crystal Growth* 101 (1990) 131.
9. J. Zhang, W. Jie, T. Wang, D. Zeng, Y. Hao and K. He, *J. Crystal Growth* 310 (2008) 3203.
10. K. Guergouri, M. S. Ferah, R. Triboulet and Y. Marfaing, *J. Crystal Growth* 139 (1994) 6.
11. A. Burger, K. Chattopadhyay, H. Chen, J. O. Nday, X. Ma, S. Trivedi, S. W. Kutcher, R. Chen and R. D. Rosemeier, *J. Cryst. Growth* 198/199 (1999) 872.
12. A. Mycielski, A. Burger, M. Sowinska, M. Groza, A. Szadkowski, P. Wojnar, B. Witkowska, W. Kaliszek and P. Siffert, *Physica Status Solidi C* 2 (2005) 1578.
13. A. Hossain, Y. Cui, A. E. Bolotnikov, G. S. Camarda, G. Yang, D. Kochanowska, M. Witkowska-Baran, A. Mycielski and R. B. James, *J. Electron. Mater.* 38 (2009) 1593.

14. K. H. Kim, G. Jeng, P. Kim, J. Choi, A. E. Bolotnikov, G. S. Camarda and R. B. James, J. Appl. Phys. 114 (2013) 063706.
15. A. Tanaka, Y. Masa, S. Seto and T. Kawasaki, J. Cryst. Growth 94 (1989) 166.
16. G. A. Carini, A. E. Bolotnikov, G. S. Camarda, G. W. Wright, and R. B. James, Appl. Phys. Lett. 88, 143515 (2006).
17. P. Rudolph, M. Neubert and M. Muhlberg, J. Cryst. Growth 128 (1993) 582.
18. H. R. Vydyanath, J. Ellsworth, J. J. Kennedy, B. Dean, C. J. Johnson, G. T. Neugebauer, J. Sepich and Pok-Kai Liao, J. Vac. Sci. Technol. B 10 (1992) 1476.
19. G. Yang, A. E. Bolotnikov, P. M. Fochuk, O. Kopach, J. Franc, E. Belas, K. H. Kim, G. S. Camarda, A. Hossain, Y. Cui, A. L. Adams, A. Radja, R. Pinder and R. B. James, J. Cryst. Growth 379 (2013) 16.
20. S. K. Swain, Y. Cui, A. Datta, S. Bhaladhare, M. R. Rao, A. Burger and K. G. Lynn, J. Cryst. Growth 389 (2014) 134.
21. E. Saucedo, P. Rudolph and E. Dieguez, J. Cryst. Growth 310 (2008) 2067.
22. S. Sen, C. S. Liang, D. R. Rhiger, J. E. Stannard, and H. F. Arlinghaus, J. Electron. Mater. 25 (1996) 1188.
23. H. G. Brion, C. Mewes, I. Hahn and U. Schäufele, J. Cryst. Growth 134 (1993) 281.
24. P. Rudolph, M. Neubert and M. Muhlberg, J. Cryst. Growth 128 (1993) 582.
25. U. N. Roy, G. S. Camarda, Y. Cui, G. Gu, R. Gul, A. Hossain, G. Yang, S. U. Egarevwe, and R. B. James, J. Cryst. Growth 128 (1993) 582.



**Figure captions:**

Figure 1. Optical photograph of the CMT ingot grown by the vertical Bridgman technique. The ingot was etched in a Saucedo solution. The wafers taken from the different positions are marked by blue vertical lines (not shown to scale).

Figure 2. Photograph of the wafers etched with a Saucedo solution, cut perpendicular to the ingot axis (left) and the corresponding IR transmission image of the full wafer with a diameter of 22 mm cut from a) bottom, b) middle and c) top of the ingot, as indicated by the vertical blue lines in Fig. 1.

Figure 3. High magnification IR transmission microscopic image of the  $\text{Cd}_{0.95}\text{Mn}_{0.05}\text{Te}$  sample, a) at magnification 5X and b) 50X. The bar on the right bottom of each image indicate the scale.

Figure 4. Microscopic scanning image of the  $\text{Cd}_{0.95}\text{Mn}_{0.05}\text{Te}$  sample, a) in reflection mode and b) in IR transmission mode. Sample dimensions:  $7.9 \times 5.6 \times 3.2 \text{ mm}^3$ .

Figure 5. High magnification IR transmission microscopic images of the  $\text{Cd}_{0.95}\text{Mn}_{0.05}\text{Te}$  sample focused at different depths. The same magnification was used for all the images.

Figure 6. Enlarged version of the square indicated in Fig. 2c.

Figure 7. High magnification IR transmission microscopic image of the grain boundary, a) focussed on the surface, b) focused at a depth along the grain boundary, and c) higher magnification image focused below the surface along the grain boundary, indicating the size of the Te inclusions.

Figure 8. X-ray topographic image of the whole wafer shown in Fig. 2b.



**Highlights**

1. CdMnTe growth by vertical Bridgman method
2. Free from Te-inclusions  $> 1\ \mu\text{m}$
3. X-ray topography

ACCEPTED MANUSCRIPT